Ion outflow and associated perpendicular heating in the cusp observed by Interball Auroral Probe and Fast Auroral Snapshot

M. Bouhram,[1] N. Dubouloz,[1,2] M. Malingre,[1] J. R. Jasperse,[3] R. Pottelette,[1] C. Senior,[1] D. Delcourt,[1] C. W. Carlson,[4] I. Roth,[4] M. Berthomier,[4] and J.-A. Sauvaud[5]

Received 28 March 2001; revised 25 June 2001; accepted 9 July 2001; published 13 February 2002

[1] The spatial properties of ionospheric ion outflows associated with perpendicular heating processes in the cusp are studied using a conjunction study from two satellites and ground radar systems. Low-energy outflowing ions are measured in a wide longitudinal range, between 13,000 and 19,000 km in altitude, over the dayside polar cap by the Hyperboloid experiment aboard the Interball Auroral Probe (AP). These observations are related to conjugate convection field measurements by the Saskatoon-Kapuskasing pair of the Super Dual Auroral Radar Network (SuperDARN). Data analysis suggests that outflowing ions originate from a wide magnetic local time range associated with both the dayside cusp region and the dayside cleft region. A direct cusp crossing by the Fast Auroral Snapshot (FAST) satellite at 2000-km altitude shows a correlation between transverse ion heating in a thin latitudinal region ($\sim$1.3°) and the presence of broadband extremely low frequency (BBELF) turbulence, in addition to more intense electrostatic waves near and just above the lower hybrid (LH) frequency. This event is unusual because on the basis of the statistical survey of Freja and FAST data, most of the ion-heating events in the midaltitude auroral zone are correlated with enhanced emissions in the BBELF range. Furthermore, the electron population has energies that are too small to drive LH waves unstable. This event offers the opportunity to analyze the contribution of cusp magnetospheric ion injections to the heating of the ambient H^+ and O^+ ions. Kinetic instability calculations demonstrate that LH waves are destabilized by the ring distributions, which result from injections of high-energy magnetosheath ions. Calculations show that a preheating mechanism by BBELF turbulence near the ion gyrofrequencies is also required so that LH heating is able to occur. The altitude dependence of the LH perpendicular heating is then analyzed by modeling the transport of the injected magnetospheric ions along magnetic field lines. It is shown that LH heating acts as an additional process from $\sim$2000 up to 10,000 km in altitude. In addition, trajectory calculations show that the low-energy outflowing H^+ and O^+ ions observed along Interball AP orbit in the polar cap are heated inside the cusp at altitudes extending up to 15,000 km. These results are then assembled to construct a possible heating scenario inside the cusp for this data set. The contribution of the different energization mechanisms to the ion heating as a function of altitude is then discussed. *INDEX TERMS:* 2704 Magnetospheric Physics: Auroral phenomena (2407); 2724 Magnetospheric Physics: Magnetopause, cusp, and boundary layers; 7859 Space Plasma Physics: Transport processes; 7867 Space Plasma Physics: Wave/particle interactions

1. Introduction

[2] It has been known for a few decades that the Earth's ionosphere acts as a significant source of magnetospheric plasma [*Moore et al.*, 1999a]. The dayside cusp/cleft region has been identified as a major source of ionospheric ions for the Earth's magnetosphere [*Lockwood et al.*, 1985b]. Previous observations by the Dynamics Explorer 1 (DE 1) satellite revealed that outflowing ions, first heated in a narrow latitudinal band in the dayside cleft region, drift into the polar cap toward the nightside sector under the effect of magnetospheric convection and forming the so-called "cleft ion fountain" [*Lockwood et al.*, 1985a]. Furthermore, other observations between 2000 and 5000 km in altitude by DE 1 [*Moore et al.*, 1986], Viking [*André et al.*, 1988], or Akebono [*Knudsen et al.*, 1994] satellites put forward evidence of transverse O^+ heating in the dayside auroral zone, where the ions overcome gravity and form fountain outflows.

[3] Because the low-energy (0–50 eV) outflowing ions have field-aligned velocities of the order of the typical convection velocities, the horizontal ion transport must be taken into consideration for a particular event so as to associate ion fountain observations with a precise location of the corresponding transverse heating processes in the dayside cusp/cleft region. A detailed knowledge of the convection field patterns can be obtained when satellite observations are correlated with convection measurements from a pair of the Super Dual Auroral Radar Network (SuperDARN) chain. Because SuperDARN convection data were not available during the period of the DE 1 or Akebono missions, the previous studies were not able to locate precisely the ion fountain

[1]Centre d'étude des Environnements Terrestre et Planétaires, Saint-Maur, France.
[2]Now at Laboratoire de Physique et Chimie de l'Environnement, Orléans, France.
[3]Air Force Research Laboratory, Hanscom Air Force Base, Massachusetts, USA.
[4]Space Science Laboratory, University of California, Berkeley, California, USA.
[5]Centre d'étude Spatiale des Rayonnements, Toulouse, France.

Copyright 2002 by the American Geophysical Union.
0148-0227/02/2001JA000091$09.00

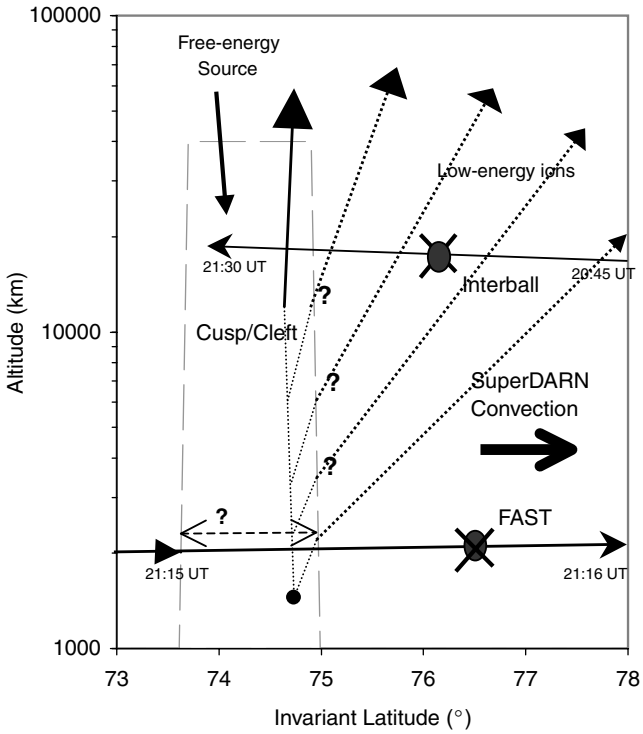

Figure 1. A sketch showing the coincidence between Interball 2, Fast Auroral Snapshot (FAST), and Super Dual Auroral Radar Network (SuperDARN) radar measurements. The trajectories are projected in the noon-midnight meridian plane and are given as functions of invariant latitude and altitude.

source region. Recently, *Dubouloz et al.* [2001] analyzed an event of ion outflow observations by the Hyperboloid ion mass spectrometer aboard Interball Auroral Probe (AP) in conjunction with convection measurements from the Saskatoon-Kapuskasing pair of SuperDARN radars. Ion trajectories were traced backward in time under the effect of macroscopic magnetic and electric fields, as described by a dipole model and SuperDARN data convection field, respectively. In this case study it was found that the observed outflowing ions originate from the cusp rather than from the cleft region.

[4] After determining the location of ion-heating processes, the next step is to understand which physical mechanisms induce the perpendicular ion heating associated with the ion outflow observations. Perpendicular heating by wave-particle interactions seems the most plausible explanation, because many candidate wave modes have been locally observed by satellites crossing the dayside cusp/cleft region. Using statistical observations from the Freja satellite, *Norqvist et al.* [1998] showed that most of the transverse ion-heating events at altitudes below 1700 km are associated with an enhancement of the broadband extremely low frequency (BBELF) turbulence. Other observations by the Fast Auroral Snapshot (FAST) satellite at altitudes below 4000 km confirm this result [*Lund et al.*, 2000]. Furthermore, Monte Carlo simulations [*André et al.*, 1990; *Norqvist et al.*, 1996] showed that such waves can cause the observed ion energies through cyclotron resonance around the ion gyrofrequencies. However, other energization mechanisms may operate in the dayside cusp/cleft region. One possibility is heating by electrostatic waves around the lower hybrid (LH) frequency. Using kinetic simulations, *Roth and Hudson* [1985] demonstrated that ion ring distributions, which have been commonly observed downflowing into the cusp on the S3-3 and DE 1 satellites at ~1–4 Earth radii, can generate LH waves locally. Such waves, in turn, can heat perpendicularly the cold ion populations by a resonant interaction between the waves and the particles.

[5] A few transverse ion heating events have been simultaneously associated with remote observations of outflowing ions. *Peterson et al.* [1993a] studied the first case where outflowing H^+ and O^+ populations were observed simultaneously on the Akebono and DE 1 satellites at altitudes ~5000 and 22,000 km along the same field line in the cusp. The data set illustrated that the energization and the transport of ions are more complex than previously anticipated, since multiple heating processes can occur. During the same event, *Peterson et al.* [1993b] used coincident observations of magnetic field perturbation to show that the structure is more consistent with an interpretation of a standing Alfvén wave than that of a field-aligned current sheet. Unfortunately, in both papers a detailed examination of the source and the wave modes inducing transverse ion heating as a function of altitude was not investigated quantitatively.

[6] The present study describes coincident observations of ion outflows, transverse ion heating, and magnetospheric convection patterns. Figure 1 shows a projection of these correlated observations in the noon-midnight meridian plane. During this event the convection is antisunward directed and therefore parallel to the noon-midnight plane. In practice, the satellite orbits are not in the same meridian plane. Therefore such a model assumes that the heating region is longitudinally uniform. Interball AP detects outflowing ions in the dayside morning polar cap at altitudes ranging from 13,000 to 19,000 km. During this event the FAST satellite crosses the polar cusp close to noon at 2000-km altitude. The coincident satellite measurements offer the opportunity to analyze the spatial properties of the ion-heating region. FAST observations provide information about the low-altitude heating processes occurring in the source region of the outflows. Using convection measurements from SuperDARN data, adiabatic trajectories backward in time from Interball AP to the poleward heating boundary provide information about the altitude extent of the heating region [*Dubouloz et al.*, 2001].

[7] The outline of the paper is as follows. In section 2 we overview the observations by Interball AP and FAST satellites for this case study and show the convection map as inferred from SuperDARN radars. In section 3 we analyze the generation of the different wave modes identified by FAST (e.g., BBELF and LH waves) and discuss the contribution of each of them in terms of ion energization. In section 4, by using ion distributions measured by FAST and modeling ion transport along magnetic field lines, we model the altitude dependence of transverse ion heating. The influence of the different heating mechanisms is discussed in section 5 with a proposed heating scenario occurring in the cusp for this case study. A summary of our conclusions is given in section 6.

2. Observations

2.1. Interball AP Data

[8] Figure 2 shows a summary plot of particle data recorded on January 17, 1998, between 1930 and 2140 UT while Interball AP traveled westward over the dayside polar cap region in the Northern Hemisphere at altitudes ranging from 13,000 to 19,000 km. At the beginning of the time interval, Interball AP was on closed plasma sheet field lines, as evidenced in Figure 2c by the dense cold isotropic H^+ population. At ~1940 UT (~6.9 magnetic local time (MLT) and 69.5° invariant latitude), ion distributions are suddenly shifted to higher energies, as evidenced by the observations of high-energy (few keV) H^+ and O^+outflows (Figures 2b and 2d), corresponding to ions heated at lower altitudes. This region is interpreted as the closed/opened field line boundary representing the morning edge of the auroral oval, characterized by high-energy magnetosheath-like electron and proton precipitation [*Newell et al.*, 1991]. After the oval crossing at 1946 UT, ion

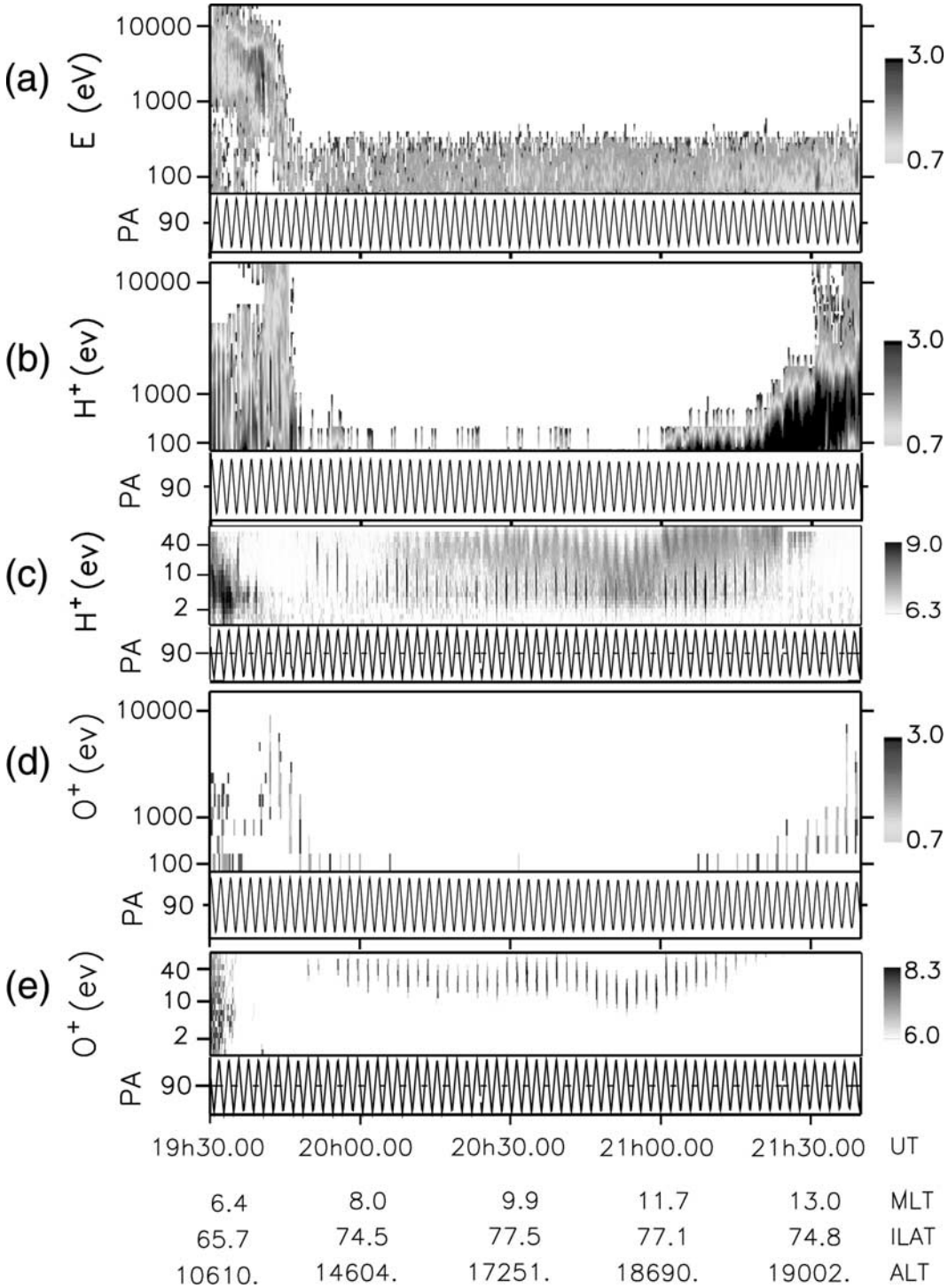

Figure 2. Energy-time spectrograms of particles aboard Interball AP on January 17, 1998, between 1930 and 2140 UT. (a) 100 eV to 10 keV electrons, (b) 100 eV to 10 keV H^+ ions, (c) 0–80 eV H^+ ions, (d) 100 eV to 10 keV O^+ ions, and (e) 0–80 eV O^+ ions. High-energy measurements in counts are from the ION experiment. Low-energy ion number fluxes in log $[(m^2\ s\ sr\ eV)^{-1}]$ are measured by the central window of the Hyperboloid experiment. The corresponding pitch angle (PA) plot is represented below each spectrogram. See color version of this figure at back of this issue.

spectrograms exhibit outflowing populations. These outflows are due to ion-heating processes occurring at both lower altitude and lower latitude in the cusp/cleft region. These outflows are observed over a broad MLT range between ~7.0 and 13.0 hours, suggesting that heating processes subsequently occur in all the morning sector in the dayside cusp/cleft region and that the ions drift by the convection into the polar cap. After 2005 UT the low-energy H^+ spectrogram detects a background population that represents the low-energy tail of the injected magnetosheath protons. For this reason the ionospheric H^+ population is less easy to identify because of mixing with this magnetosheath population. The fact that the time-energy dispersion of H^+ and O^+ outflowing ions is

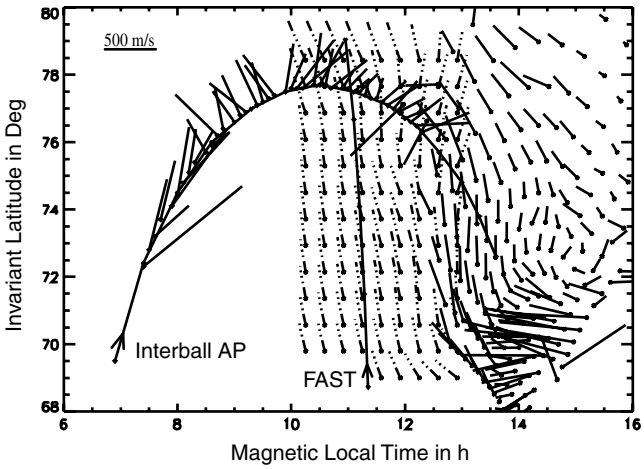

Figure 3. Convection map between 2020 and 2120 (UT). Solid line vectors are deduced from the radar observations. The projections of Interball AP and FAST footprints are indicated. Along Interball AP orbit, the convection velocity vectors are deduced from the average perpendicular velocities of O^+ ions measured by Hyperboloid. Dashed line vectors deduced from a convection model are superposed in regions where the convection is not measured.

the same as that for the precipitating H^+ population could be basically explained by the satellite trajectory relative to the horizontal transport of ions due to the convection [*Dubouloz et al.*, 2001]. At ~2048 UT (~11.0 MLT and 77.5° invariant latitude) the time-energy modulation breaks off, with a gradual increase of the average energy of the outflowing population, which is accompanied by enhanced fluxes of the magnetosheath protons. The heating regions that are the origin of the outflowing ions observed before and after 2048 UT may be different in nature. Because statistically precipitating ion fluxes in the cusp are higher than those anywhere else in the auroral oval [*Newell et al.*, 1991], we show later that the enhanced magnetosheath number fluxes of $\sim 3 \times 10^8$ (m^2 s sr eV)$^{-1}$ with energies around 10 eV are also consistent with a proton population injected into the cusp and transported by the antisunward convection to the Interball AP orbit. For this reason, this discontinuity may be associated with the transition region between observed ion outflows from the cleft and observed ion outflows from the cusp. After 2126 UT (~12.8 MLT and 75.2° invariant latitude), ion distributions are slowly shifted to higher energies, indicating the entry in the cusp proper, as evidenced by high-energy protons from magnetosheath and electron fluxes with moderate energies on Figure 2a and 2b. Inside the cusp, outflowing H^+ and O^+ ions are detected with significant energies extending up to a few keV. This suggests that strong heating processes occurred in a wide altitude range below the satellite.

2.2. Convection Data

[9] Because the ion field-aligned velocities are comparable to the convection velocities, a detailed knowledge of the convection field is crucial to obtain a correct interpretation of the observed time-energy dispersion and to locate the heating region. Several approaches have been used to construct a detailed and realistic model of convection patterns. During this event, Interball AP crosses the common field of view of the Saskatoon-Kapuskasing pair of the SuperDARN chain. Radars provide in their common field of view a convection map in a plane perpendicular to the geomagnetic field in *F* region [*Greenwald et al.*, 1995]. Figure 3 displays the constructed convection map. Because the convection seems to be in a steady state in a reference frame relative to the Sun's direction, data have been integrated for 1 hour to reproduce the plasma velocity vectors. Combined data show a convection mostly antisunward, consistent with the southward direction of the interplanetary magnetic field (IMF). Wind satellite measurements show a southward B_z varying from −4 to −2 nT and a positive B_y about 1 nT. The shape of the convection patterns confirms that the observed H^+ and O^+ outflowing ions originate from a wide MLT range in the dayside cusp/cleft region.

2.3. FAST Data

[10] During the event the Fast Auroral Snapshot (FAST) Explorer crossed the morningside edge of the cusp with an antisunward polar orbit near noon (11.2 MLT), at an altitude ~2000 km in the Northern Hemisphere. Figure 4 displays a set of particle and waves measurements recorded on FAST between 2114:25 and 2116:05 UT. A description of the FAST satellite and instruments can be found in the work of *Carlson et al.* [1998]. The particle data displayed in Figure 3 are measured in a half-plane containing the geomagnetic field $\mathbf{B_0}$ and opposite to the ram direction.

[11] Between 2114:50 (~73.7° invariant latitude) and 2115:15 (~74.7° invariant latitude), both electron energy and pitch angle spectra indicate an isotropic electron population with energy fluxes $\sim 10^9$ eV (cm^2 s sr eV)$^{-1}$ and moderate energies below 100 eV. In the same interval, ion energy spectra (Figure 4c) show a region of direct magnetosheath plasma entry with energies below 1 keV and strong energy fluxes also ($\sim 5 \times 10^7$eV (cm^2 s sr eV)$^{-1}$). These electron and ion characteristics are typical of the cusp region [*Newell and Meng*, 1988]. In addition, energy fluxes of the low-energy tail (few tens of eV) of the magnetosheath population $\sim 7 \times 10^5$ eV (cm^2 s sr eV)$^{-1}$ observed by FAST after 2114:45 UT approximately correspond to energy fluxes from the same population observed by Interball AP at ~2052 UT in the same sector (see Figure 2c) but at a higher altitude. Between 2115:00 and 2115:10 UT, intense energy fluxes of warm (a few tens of eV) ions are observed in Figures 4c and 4d, with pitch angles from 90° to 110°. These observations indicate a thin region, ~1.3° invariant latitude (~140 km) of transverse ion heating. This is in agreement with the heating wall concept [*Knudsen et al.*, 1994], suggesting that ionospheric ions are suddenly heated transversely to $\mathbf{B_0}$ in a narrow latitudinal region, then overcome gravity via the mirror force, and are swept by the convection outside this region.

[12] The region of intense ion heating identified by particle data is correlated with a strong activity of high-frequency electrostatic waves (Figures 4f and 4g) that propagate in a wide frequency range between 2.4 and 300 kHz. Strong peaks are observed close to lower- and upper-frequency limits of this emission. The lower limit can be interpreted as the lower hybrid (LH) frequency (Figure 4g), which corresponds to waves propagating with a wave vector perpendicular to $\mathbf{B_0}$. Because the electron gyrofrequency (~735 kHz) is higher than 300 kHz, the upper limit represents the electron plasma frequency (Figure 4f), which corresponds to waves propagating with a wave vector parallel to $\mathbf{B_0}$. The densities of the different species (H^+ and O^+) can be inferred from the value of the electron plasma frequency (~300 kHz) and the ratio between this frequency and the LH frequency. We found a total density n_e= 1100 cm^{-3} with a 90% O^+-dominated plasma. In Figure 4g a third frequency domain of intense broadband extremely low frequency (BBELF) turbulence is observed inside the heating region at lower frequencies below 400 Hz. Narrowband emissions around the proton gyrofrequency (400 Hz) are observed inside and outside the heating region, with approximately the same intensity.

[13] Figure 5 provides a closer look of the ion distribution inside the heating region at 2115:05 UT. The ion space-velocity distribution was obtained from all the detectors in a plane perpendicular to the spin axis and containing $\mathbf{B_0}$ and was reproduced in the plasma frame by subtracting both convection and satellite speeds. This distribution is dominated by a mixed H^+ and O^+ ion conic with a small upward parallel drift and perpendicular velocities

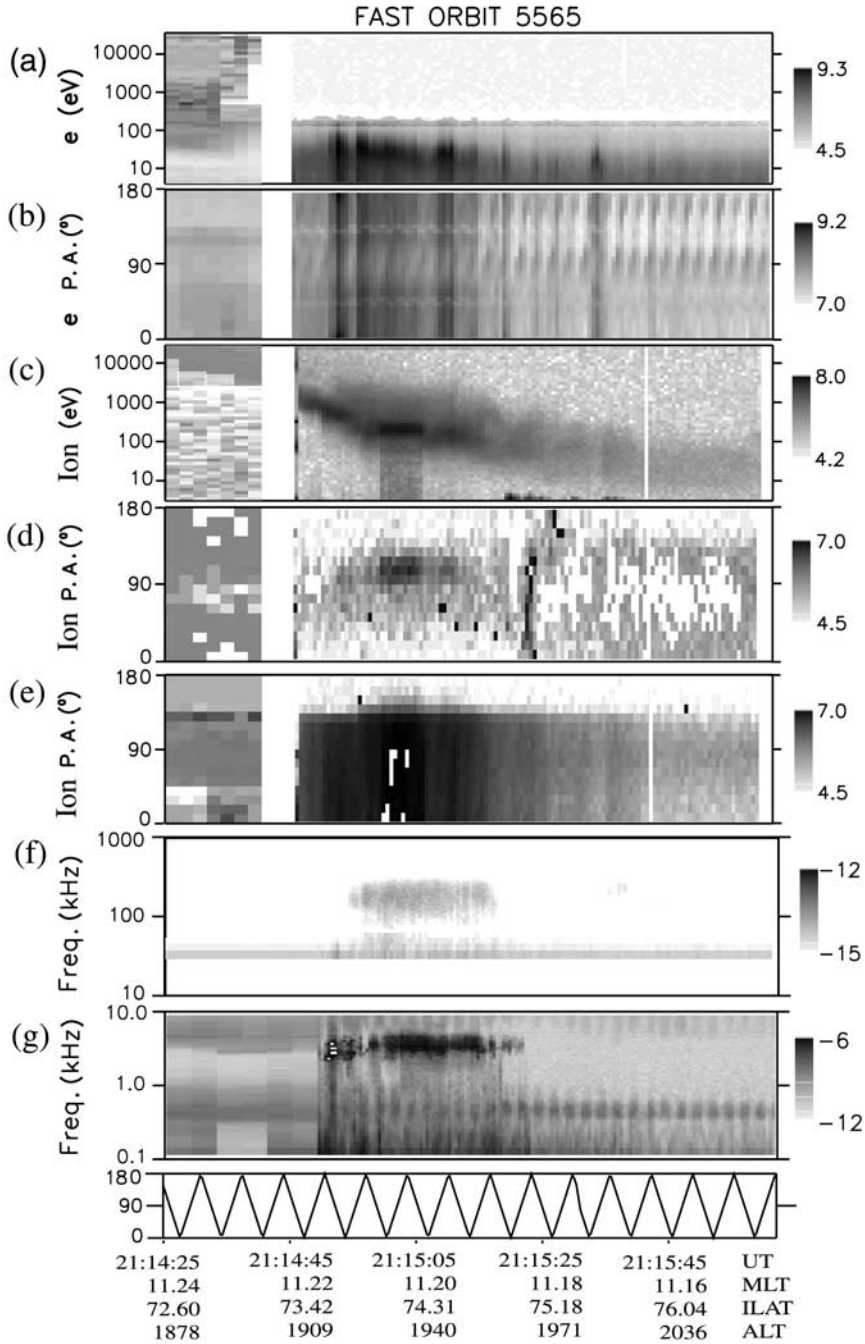

Figure 4. FAST observations of a cusp crossing on January 17, 1998, between 2114:25 and 2116:05 UT. (a) The electron energy spectra from 3 eV to 30 keV for all pitch angles, (b) the electron pitch angle spectra for all energies, (c) the ion energy spectra from 3 eV to 30 keV for all pitch angles, (d) the ion pitch angle spectra integrated over energies below 20 eV, and (e) the ion pitch angle spectra integrated over energies above 60 eV. All particle energy fluxes are in log [eV (cm^2 s sr eV)$^{-1}$]. Note that fluxes near 180° are upgoing and those near 0° are downgoing. (f) The high-frequency electric field wave power spectrum and (g) the low-frequency perpendicular electric field wave spectrum. All wave spectra are in log [V^{2}m^{-2} Hz^{-1}]. The angle between the antenna and the geomagnetic field is shown below the spectra. See color version of this figure at back of this issue.

extending up to ~150 km s^{-1}. A horseshoe-shaped distribution is also present at higher velocities around 230 km s^{-1}. Such a distribution results from magnetosheath injections of protons and a few percentages of He^{++} particles into the polar cusp. This distribution has a parallel beam-like component with a wing extending into the perpendicular domain due to the mirror force and an atmospheric loss cone in the outgoing direction. This distribution has a horseshoe shape in a $V_{//}$-$V_{\perp}$ diagram but looks like a ring in the perpendicular velocity space after integrating over parallel velocities. Such distributions are usually called ring distributions [see *Gorney*, 1983; *Roth and Hudson*, 1983,1985] rather than horseshoe distributions [*Bingham et al.*, 1999] in the literature.

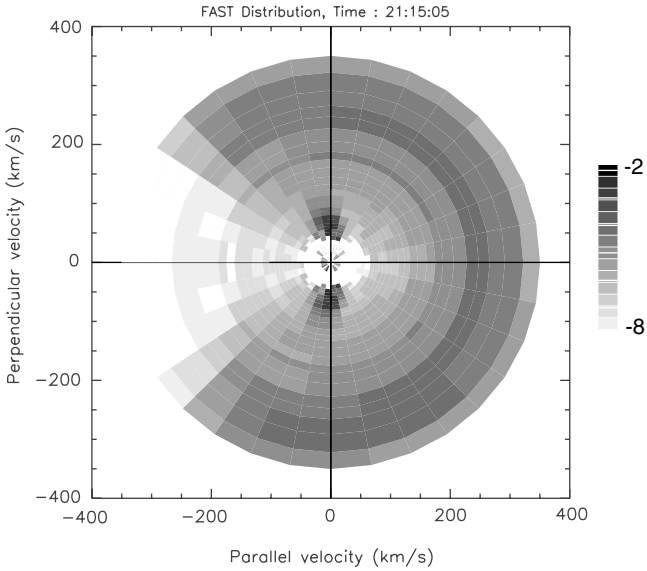

Figure 5. Ion distribution in log [cm^{-3} km^3 s^{-3}] in the plasma frame as a function of parallel and perpendicular velocity observed by FAST between 2115:03 and 2115:08 UT.

Gorney [1983] demonstrated that ring distributions contain a source of free energy able to generate wave instabilities.

3. Wave Generation and Transverse Ion Heating

[14] Figure 6 shows the perpendicular electric field spectrum obtained inside the heating region. For comparison the spectrum outside the heating region is displayed. The heating region identified with particle data is correlated with an increase of the BBELF turbulence from a few to a few hundred hertz and the presence of intense electrostatic waves around the LH frequency. Narrowband electromagnetic ion cyclotron (EMIC) emissions are also observed just below the proton gyrofrequency inside and outside the heating region, but their amplitudes are ~3 orders of magnitude smaller than LH emissions. Therefore only the BBELF and LH spectral regions should contribute to ion heating. Since these waves have different properties, we have to analyze their contributions separately. LH waves can be destabilized in different ways, by downgoing auroral electron beams with energies about several hundreds of eV [*Chang and Coppi*, 1981] or by precipitating ions with a ring-shaped distribution [*Roth and Hudson*, 1983; *Akimoto et al.*, 1985]. For this case study, the electron population has no beam to drive the LH waves unstable. Therefore we present a stability analysis of ion ring distributions in section 3.1. In section 3.2 we discuss the nature and the generation of BBELF waves, which are also correlated with ion heating. In section 3.3we emphasize the importance of the two spectral regions (e.g., BBELF and LH) in terms of transverse ion energization at FAST altitude.

3.1. Generation of LH Waves by Ion Ring Distributions

[15] The name and values of plasma parameters at FAST altitude are summarized in Table 1. Referring to the observations, this theoretical calculation includes a cold H^+ and O^+ Maxwellian background with thermal velocities u_H and u_O and densities n_H and n_O, respectively, which describes the ionospheric population before the heating. In addition, the model includes the observed H^+ ring distribution (see Figure 6), while the electrons form a cool isotropic population. The same kind of linear instability analysis was performed by *Roth and Hudson* [1983, 1985] in a multi-component plasma with H^+ as the major specie. Different analytical models for the H^+ and He^{++} ring distributions were considered. However, they studied the dispersion relation only for perpendicular wave vectors, and they neglected the electron contribution to the dynamics of the interaction. In the present analysis we consider electrostatic modes with the wave vector $\boldsymbol{k}$ approximately perpendicular to the geomagnetic field $\mathbf{B_0}$, i.e., $k_{//} \ll k_\perp$. The response of plasma to small perturbations is given by the dielectric function $\varepsilon(\mathbf{k}, \omega)$, which can be expressed as

$$\varepsilon(\mathbf{k}, \omega) = 1 + \chi_e + \chi_i + \chi_r, \tag{1}$$

where χ_e, χ_i, and χ_r are the cool electron, cold ion, and hot ring ion susceptibilities, respectively. We consider perpendicular wavelengths of the order of the ion gyroradius and therefore greater than the electron gyroradius (strongly magnetized electrons). In such a case the electron susceptibility in the limit $\omega/k_{//} \gg u_e$ can be expressed as

$$\chi_e(\mathbf{k}, \omega) = \frac{\omega_{pe}^2}{\omega_{ce}^2} - \frac{\omega_{pe}^2}{\omega^2} - \frac{k_{//}^2}{k^2}\left(1 + \frac{k_{//}^2 u_e^2}{\omega^2}\right). \tag{2}$$

[16] The cold ion susceptibility for a Maxwellian distribution in a magnetized plasma is given by

$$\chi_i(\mathbf{k}, \omega) = \sum_{i=\mathrm{H,O}} 2\omega_{pi}^2 e^{-\beta_i} \Big/ \beta_i \sum_n \frac{n^2 I_n(\beta_i)}{\omega^2 - n^2\omega_{ci}^2} \tag{3}$$

with $\beta_i = k_\perp^2 \rho_i^2 = k_\perp^2 u_i^2/\omega_{ci}^2$ and for the hot ring distribution the susceptibility is given by

$$\chi_e(\mathbf{k}, \omega) = 2\pi \frac{\omega_{pr}^2}{k_\perp^2} \sum_n \frac{2n^2\omega_{cr}^2}{\omega^2 - n^2\omega_{cr}^2} \int_0^{+\infty} J_n^2(\xi) f_\perp'(\xi) d\xi, \tag{4}$$

where I_n and J_n are Bessel functions [*Abramowitz and Stegun*, 1964] and $\xi = k_\perp V_\perp/\omega_{cr}$. In this formula, $f_\perp$ represents the ring-shaped distribution function after integrating over the parallel velocity $V_{//}$. Because the ring density verifies $n_r < n_H \ll n_O$, the ring term contributes slightly to the real part of $\varepsilon(\mathbf{k}, \omega)$. Details of

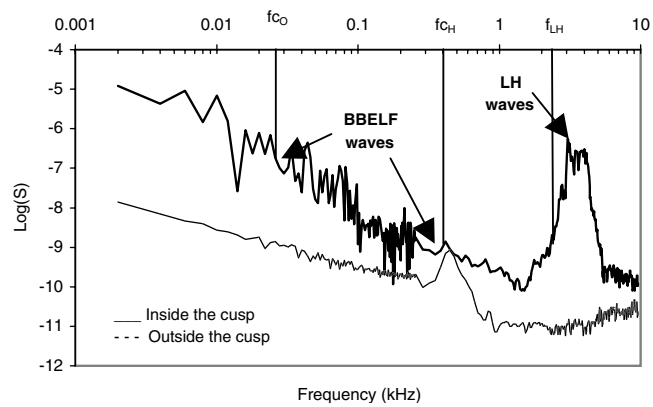

Figure 6. The observed perpendicular wave power spectrum between 0.01 and 10 kHz, inside the heating region at 2115:05 UT (solid curve) and outside the heating region at 2115:30 UT (dashed curve). BBELF, broadband extremely low frequency; LH, lower hybrid.

Table 1. List and Values of Numerical Parameters at FAST Altitude[a]

Definition	Notation	Value
FAST altitude, km	z	2,000
Electron density, cm^{-3}	n_e	1,100
Electron thermal velocity, km s^{-1}	u_e	1,300
O^+ density, cm^{-3}	n_O	1,000
O^+ thermal velocity, km s^{-1}	u_O	2.5
H^+ density, cm^{-3}	n_H	80
H^+ thermal velocity, km s^{-1}	u_H	10
Ring density, cm^{-3}	n_r	20
Electron plasma frequency, kHz	f_{pe}	300
H^+ plasma frequency, kHz	f_{pH}	1.9
O^+ plasma frequency, kHz	f_{pO}	1.7
Ring plasma frequency, kHz	f_{pr}	0.94
Genetic field, μT	B_0	27
Electron cyclotron frequency, kHz	f_{ce}	735
H^+ cyclotron frequency, Hz	f_{cH}	400
O^+ cyclotron frequency, Hz	f_{cO}	25
Lower hybrid frequency, kHz	f_{LH}	2.4
Two-ion hybrid frequency, Hz	f_B	250
Electron gyroradius, m	ρ_e	0.1
O^+ gyroradius, m	ρ_O	16
H^+ gyroradius, m	ρ_H	4
Ring gyroradius, m	ρ_r	100
Parallel phase velocity, km s^{-1}	$\omega/k_{//}$	~15,000
Perpendicular phase velocity, km s^{-1}	$\omega/k_\perp$	60–240

[a] The moments of the different constituents and the specific frequencies are inferred from particle and wave data on Fast Auroral Snapshot (FAST).

the calculation in (2), (3), and (4)are available from *Krall and Trivelpiece* [1986].

[17] In the regime $\omega > \omega_{cr} = \omega_{cH}$, at long wavelengths $k_\perp\rho_H \ll 1$ and by neglecting the real part of χ_r, the mode $n = 1$ corresponds to the LH mode:

$$\omega_+ = \omega_{LH}\sqrt{1 + M\,k_{//}^2\Big/k^2}, \tag{5}$$

where ω_{LH} is the LH frequency given by

$$\omega_{LH} = \omega_{pe}\Big/\sqrt{M\left(1 + \omega_{pe}^2\Big/\omega_{ce}^2\right)}, \tag{6}$$

and $M = (n_e/m_e)/(n_i/m_i)$ is an effective ion mass normalized with respect to the electron mass. Because in the cusp region, $\omega_{pi}^2 \gg \omega_{ci}^2$, the value of ω_{LH} is not sensitive to the ion gyrofrequencies. However, since $\omega_{LH} > \omega_{cH}$, this value falls between two adjacent values of hydrogen gyroharmonics and may destabilize some wave numbers (as shown later). Because for small values of $k_\perp\rho_H$, Bessel functions of higher orders are smaller, the other modes $n > 1$ are hardly sensitive to hydrogen gyroharmonics $n\omega_{cH}$.

[18] In the lower-frequency regime, $\omega < \omega_{cr} = \omega_{cH}$, both hydrogen and ring susceptibilities become ω independent. At long wavelengths and for $k_{//} = 0$ the oxygen mode $n = 1$ corresponds to the ion-ion hybrid mode $\omega = \omega_B$, where ω_B is the ion-ion hybrid frequency given by

$$\omega_B^2 = \omega_{pO}^2\Big/\left(1 + \omega_{pe}^2\Big/\omega_{ce}^2 + \omega_{pH}^2\Big/\omega_{cH}^2 + \omega_{pr}^2\Big/\omega_{cr}^2\right) + \omega_{cO}^2. \tag{7}$$

At FAST altitudes, $\omega_{pO} \gg \omega_{cO}$; therefore the value of ω_B mainly depends on the oxygen contribution to the plasma density. Because oxygen gyroharmonics are less separated than hydrogen gyroharmonics, this mode is propagating over several oxygen gyroharmonics. For the same reason as for hydrogen modes, the other oxygen modes $n > 1$ are close to the oxygen gyroharmonics $n\omega_{cO}$.

[19] The LH instability results from a coupling between both hydrogen modes $n = 1$ and $n = \nu$. Therefore the corresponding solution of the dispersion relation is near $\omega = \nu\omega_{cH} + i\gamma$, where γ denotes the growth rate of the unstable mode. By keeping only the $n = 1$ and $n = \nu$ terms in both ion and ring susceptibilities and by neglecting the ion Landau damping, the growth rate γ for $k_{//} = 0$ can be expressed as

$$\gamma = \frac{\nu\omega_{cH}\omega_{pr}}{k_\perp}\sqrt{\pi\int_0^{+\infty} J_\nu^2(\xi)f_\perp'(\xi)d\xi}. \tag{8}$$

The instability occurs when the integration is positive, i.e., when $f_\perp(V_\perp)$ has a positive slope, this condition determining the range of unstable perpendicular wave numbers.

[20] Numerical solutions of the dispersion relation have been carried out for the observed ring distribution and the plasma parameters, as listed in Table 1. Figure 7 displays the dispersion relation solutions when $\mathbf{k}\perp\mathbf{B_0}$ ($k_{//} = 0$). In such a case the LH mode couples to the $n = 5$–6 (2–2.4 kHz) hydrogen harmonics. The maximum growth rate is weak about $0.05\omega_{cH}$ at $k_\perp\rho_H = 0.45$. In the low-frequency diagram (Figure 7b) the ion-ion hybrid mode is propagating over several oxygen gyroharmonics between $10\omega_{cO}$ and $16\omega_{cO} = \omega_{cH}$ (250–400 Hz), but there is no instability. Figure 8 shows the dispersion relation solution for waves with a small $k_{//}$ component. Both unstable frequencies and growth rate features are modified. For $k_{//}/k = M^{-1/2}$ the LH mode couples to the $n = 7$–8 (2.8–3.2 kHz) hydrogen harmonics and is unstable between $0.4 < k_\perp\rho_H < 0.8$. The maximum growth rate occurs for $k_\perp\rho_H = 0.65$ and is more significant than that for $k_{//} = 0$ case. The variation of the maximum growth rate and the corresponding frequency as a function of $k_{//}$ are displayed in Figure 9. For $k_{//} > 0$ this maximum growth rate occurs between $0.5 < k_\perp\rho_H < 0.6$. The real frequency is close to the analytical expression given by (5). According to the

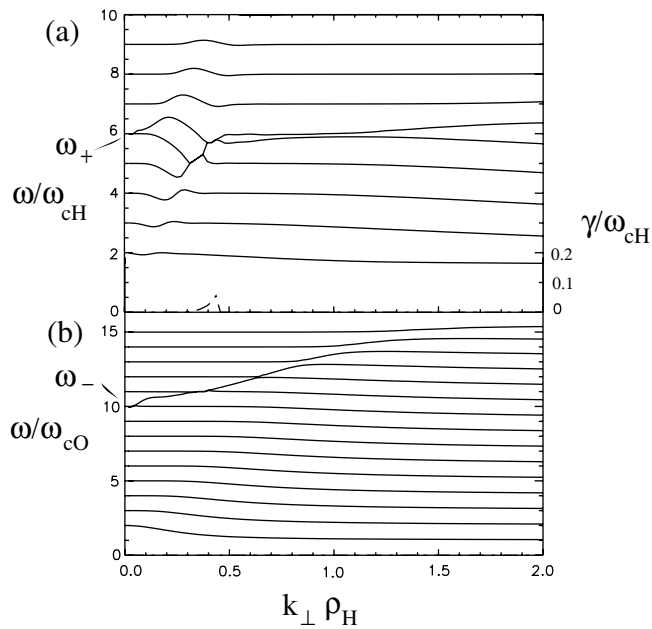

Figure 7. Solution of the dispersion relation at FAST altitude for waves propagating perpendicularly to the magnetic field ($\mathbf{k}_{//} = 0$) in (a) the high-frequency regime ($\omega > \omega_{cH}$) and (b) in the low-frequency regime ($\omega < \omega_{cH}$). The solid curves indicate ω/ω_{cH}, and the dashed curve indicates γ/ω_{cH}.

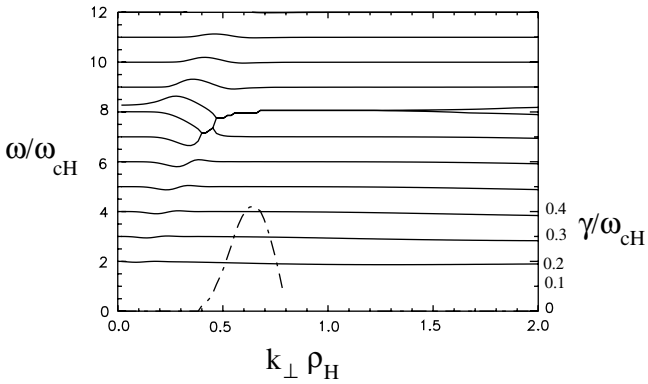

Figure 8. Plot of the dispersion relation at FAST altitude for $k_{//}/k = M^{-1/2}$. The solid curves indicate ω/ω_{cH}, and the dashed curve indicates γ/ω_{cH}.

observed wave spectrum above the LH frequency, a broad range of frequencies from $\omega_{LH} \sim 5\omega_{cH}$ to $2\omega_{LH} \sim 10\omega_{cH}$ is unstable, and the maximum growth rate increases versus $k_{//}$ and ω. For higher values of $k_{//}$ the growth rate falls off because of electron Landau damping. This branch is not displayed in our model, because of the assumption in (2) that $\omega/k_{//} \gg u_e$ breaks down when the damping occurs.

3.2. BBELF Turbulence

[21] During this event, transverse ion heating is correlated with enhanced BBELF emissions. This turbulence may contain several wave modes; its true nature is currently under investigation. Possible wave mode candidates include velocity-shear-driven ion cyclotron waves [*Amatucci et al.*, 1998], narrowband electromagnetic ion cyclotron (EMIC) waves [*Erlandson et al.*, 1994], slow ion acoustic waves [*Wahlund et al.*, 1998], and inertial Alfvén waves Doppler-shifted by the satellite motion [*Staciewicz et al.*, 2000]. Each of these wave modes may explain part of the BBELF spectrum, depending on each event and the magnetospheric regions. However, we do not attempt to explain what drives the BBELF turbulence in our case study, which is beyond the scope of the paper. Concerning transverse ion heating, the theory of cyclotron resonance heating by electromagnetic left-hand circular polarized (LHCP) waves around the ion gyrofrequencies [*Chang et al.*, 1986] seems the most efficient mechanism. This is confirmed by Monte Carlo simulations [*Norqvist et al.*, 1996], which showed that only a small fraction of the BBELF turbulence is sufficient to explain the observed ion energies through ion cyclotron resonance by the LHCP component. In the following we assume that BBELF heating occurs because of a resonant interaction between ionospheric ions and the LHCP component of the BBELF turbulence.

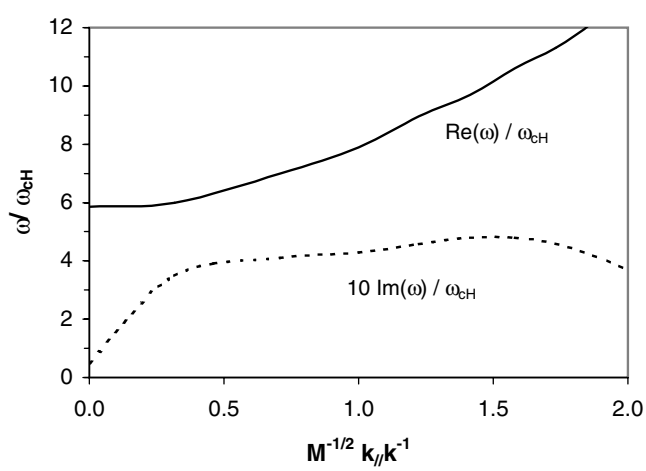

Figure 9. Solution of the dispersion relation versus $k_{//}/k$ for fixed $k_{\perp}$. The solid curve indicates ω/ω_{cH}, and the dashed curve indicates 10 γ/ω_{cH}.

3.3. Ion-Heating Rates

[22] Many properties of the ion energization at FAST altitude can be understood by estimating the ion-heating rates produced by the different wave mechanisms. The ion-heating rate associated with LHCP ion cyclotron waves leads to the model [*Chang et al.*, 1986]

$$W_{IC} = \left(q_i^2/2m_i\right) \times \eta_L S(f_{ci}), \tag{9}$$

where q_i and m_i are the ion charge and mass. $S(f_{ci})$ denotes the electric field spectral density of the BBELF waves at the ion gyrofrequency, and η_L denotes the fraction of $S(f_{ci})$ in the LHCP ion cyclotron component.

[23] The ion-heating rate for LH waves can be expressed as [see *Retterer et al.*, 1989; *André et al.*, 1994]

$$W_{LH} = \left(q_i^2/2m_i\right) \times S_{LH} \times (V_{\perp}/V_0)^3 \Big/ \left[1 + (V_{\perp}/V_0)^6\right], \tag{10}$$

where S_{LH} is the spectral density around the LH frequency f_{LH} (see Figure 6). The parameter $V_0 \sim 150$ km s^{-1} represents the phase velocity of waves observed near the peak and roughly corresponds to the unstable velocity which provides a maximum growth rate.

[24] Figure 10 provides the heating rate profiles versus perpendicular velocity $V_{\perp}$ using the measurements of electric spectral densities aboard FAST. For the LHCP ion cyclotron waves we assumed $\eta_L = 10\%$. The ion cyclotron heating is more efficient in heating O^+ions than in heating H^+ ions. For O^+ ions, LH and ion cyclotron heating rates are about the same order of magnitude. This is not the case for H^+ ions, where the maximum LH-heating rate is found several orders of magnitude

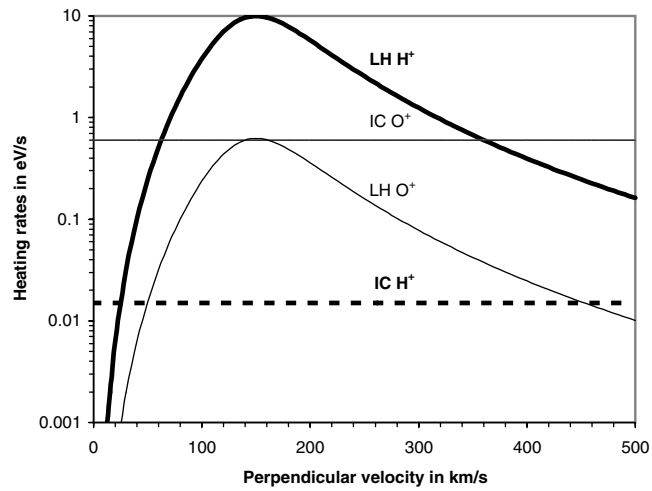

Figure 10. Heating rate profiles of H^+ (thick lines) and O^+ (thin lines) ions as a function of perpendicular velocity. The dashed lines indicate the heating rate associated with electromagnetic left-hand circular polarized (LHCP) ion cyclotron (IC) waves, and the solid curves indicate the heating rate associated with LH waves.

greater than the ion cyclotron heating rate. Furthermore, since the LH perpendicular wavelengths (few tens of meters) are lower than the antenna length (56 m), the measured value of S_{LH} may be underestimated by one order of magnitude [see *Bell et al.*, 1991]. However, Figure 10 shows that there is a threshold effect of the LH-heating rate profile versus $V_\perp$. Therefore BBELF waves are needed to accelerate the ionospheric H^+ and O^+ ions up to a few tens of km s^{-1}, so that LH heating becomes efficient at and above the FAST altitude. By assuming that the heating rate inferred is the same at lower altitudes from 1000 to 2000 km, an approximate calculation may show that preheating by the LHCP component of the BBELF waves is sufficient. If we take an averaged ion parallel drift $\sim$3 km s^{-1} consistent with FAST observations, the average time of flight for reaching the FAST altitude is $\sim\Delta t$ $\sim$ 300 s. The corresponding perpendicular ion energization is given by $\Delta E_\perp = W_{IC}\Delta_t$, corresponding to a velocity increase $\Delta V_\perp = (2\Delta E_\perp/m_i)^{1/2}$. This calculation leads to a perpendicular velocity increase of 30 and 50 km s^{-1} for H^+ and O^+, respectively. Such values seem sufficient compared to the LH-heating rate profile.

4. Spatial Properties of the Heating Region

[25] It was shown in the section 3 that preheating by the BBELF turbulence below FAST altitudes raises the ion temperature enough so that LH heating becomes important. In the following we analyze the spatial properties of transverse ion heating. In this way an altitude model for the ion ring distributions is performed in order to determine the altitude dependence of LH heating. Furthermore, we remotely analyze the heating region by retracing trajectories of the outflowing ions from the Interball AP orbit to the poleward cusp. The reconstruction of the low-energy part of the ion distribution along the poleward heating boundary provides additional information about the altitude dependence of transverse ion heating.

4.1. An Altitude Model for Ion Injections

[26] The ring distribution is known to result from magnetosheath injections [*Burch et al.*, 1982]. The basic idea is that a proton beam with bulk velocity V_b and thermal velocity V_0 is injected into the polar cusp at an altitude $\sim$7–8 Earth radii ($\sim$50,000 km). This distribution is then converted into an ion ring distribution at lower altitudes by conservation of both energy and the first adiabatic invariant. The values of V_b, V_0, and the beam density n_b are adjusted so as to reproduce the characteristics of the ring distribution at FAST altitude. We took as input parameter a Maxwellian beam, with V_b = 230 km s^{-1}, V_0 = 30 km s^{-1}, and $n_b = 2 \times 10^{-3}$ cm^{-3}. This distribution function is then sampled with a set of test particles, each of them having a specific weight corresponding to the phase space density. The adiabatic motion of these test particles was computed. The macroparticle trajectories were absorbed upon entering into the topside ionosphere at 400-km altitude or at 50,000-km altitude for reflected particles. This model does not include the effects of time-dependent reconnection, parallel electric fields, or self-consistent wave-particle interactions. However, by performing adiabatic simulations, *Onsager et al.* [1993] justified that this zeroth-order process is sufficient to reproduce ion distributions in the low-altitude cusp. In our case study, according to the convection data, the trajectory tracing was performed by taking an antisunward convection drift velocity V_D = 250 m s^{-1} at 400-km altitude, corresponding to an electric field E_D = 14 mV m^{-1}. Actually, since injected ions have a short time of flight ($\sim$3 min) to reach the ionosphere, the injected distribution is weakly dispersed ($\sim$0.3° latitude) by the convection.

[27] TThe results of the simulation are summarized in Figure 11. *Gorney* [1983] analyzed the stability of ring distribution with data recorded on the S3-3 satellite and showed that the ring distribution is a source of free energy responsible of ion mode instabilities. In particular, the distribution displays in two regions of positive $\partial f/\partial V_\perp$ perpendicular gradient providing free energy: Region 1 is the atmospheric loss cone (LC) in the ring at lower perpendicular velocities, and region 2 is the ring core (RC) with velocities perpendicular to $\mathbf{B_0}$. These two regions when present enable us to explain the shape of the different regions providing free energy in Figure 11e.

[28] For an altitude below 1000 km, downgoing particles are absorbed into the atmosphere, and there are no upgoing particles, which yields no unstable velocities. At altitudes ranging from 1000 to 5000 km, a wide LC is formed (>30°), and the number of mirroring particles in the RC is dominant. Therefore the perpendicular unstable velocities in the LC boundary are close to the unstable velocities due to the RC, yielding a single, broad range of unstable perpendicular velocities varying from 60 to 230 km s^{-1}.

[29] For an altitude ranging from 5000 to 10,000 km the loss cone becomes narrow and therefore far from the ring perpendicular domain. This induces two separate ranges of perpendicular unstable velocities in Figure 11e.

[30] The number of locally mirroring particles decreases versus increasing altitude; this results in smaller positives $\partial f_\perp/\partial V_\perp$ slopes due to the ring at higher altitudes. Therefore, for an altitude higher than 10,000 km the number of mirroring particles in the RC is insignificant to provide free energy. This yields a single domain of unstable perpendicular velocities due to the LC boundary. Since the aperture angle of the LC decreases versus altitude, the corresponding range of unstable perpendicular velocities also decreases versus altitude.

4.2. Outflowing Ion Transport

[31] After being accelerated perpendicularly to the geomagnetic field in a narrow latitudinal region in the cusp/cleft, the ions leave this region and are transported adiabatically up to Interball AP orbit under the effect of magnetospheric convection. Outside the heating region the motion of these ions is only adiabatic, including the mirror force, gravity, and the convection drift. In this section we calculate the transport of the outflowing ions backward in time between Interball AP orbit and the poleward heating boundary, using a dipole model for the geomagnetic field, and the convection electric field from SuperDARN data (see *Dubouloz et al.* [2001] for details of this technique). We assume that this boundary is latitudinally homogeneous and located at an invariant latitude Λ = 75°, as confirmed by FAST observations. The ion distributions displayed between 2046:00 and 2116:00 UT were sampled with a set of test particles, which were traced backward in time from Interball AP orbit toward the ionosphere. The particle trajectories were stopped at the poleward heating boundary.

[32] Figure 12 shows the energy-altitude (top) and pitch angle-altitude (bottom) distributions of O^+ and H^+ ions along the poleward boundary of the heating region. The corresponding plots can show the macroscopic effect of ion heating integrated over the transit of the observed ions across the heating wall. These plots show that the observed low-energy outflowing ions are heated in a wide range of altitudes and left the acceleration region at altitudes up to 15,000 km.

[33] The O^+ pitch angle-altitude plot shows that pitch angles are found near 90° at low altitude and gradually fill a wider range as altitude increases, so that all values between 90° and 170° are covered between 5000 and 10,000 km. This result is consistent with an altitude cumulative perpendicular heating with gradual transfer from perpendicular to parallel energy via the mirror force. The cumulative heating scenario is less evident on the H^+ pitch angle-altitude plot, probably owing to the additional presence of

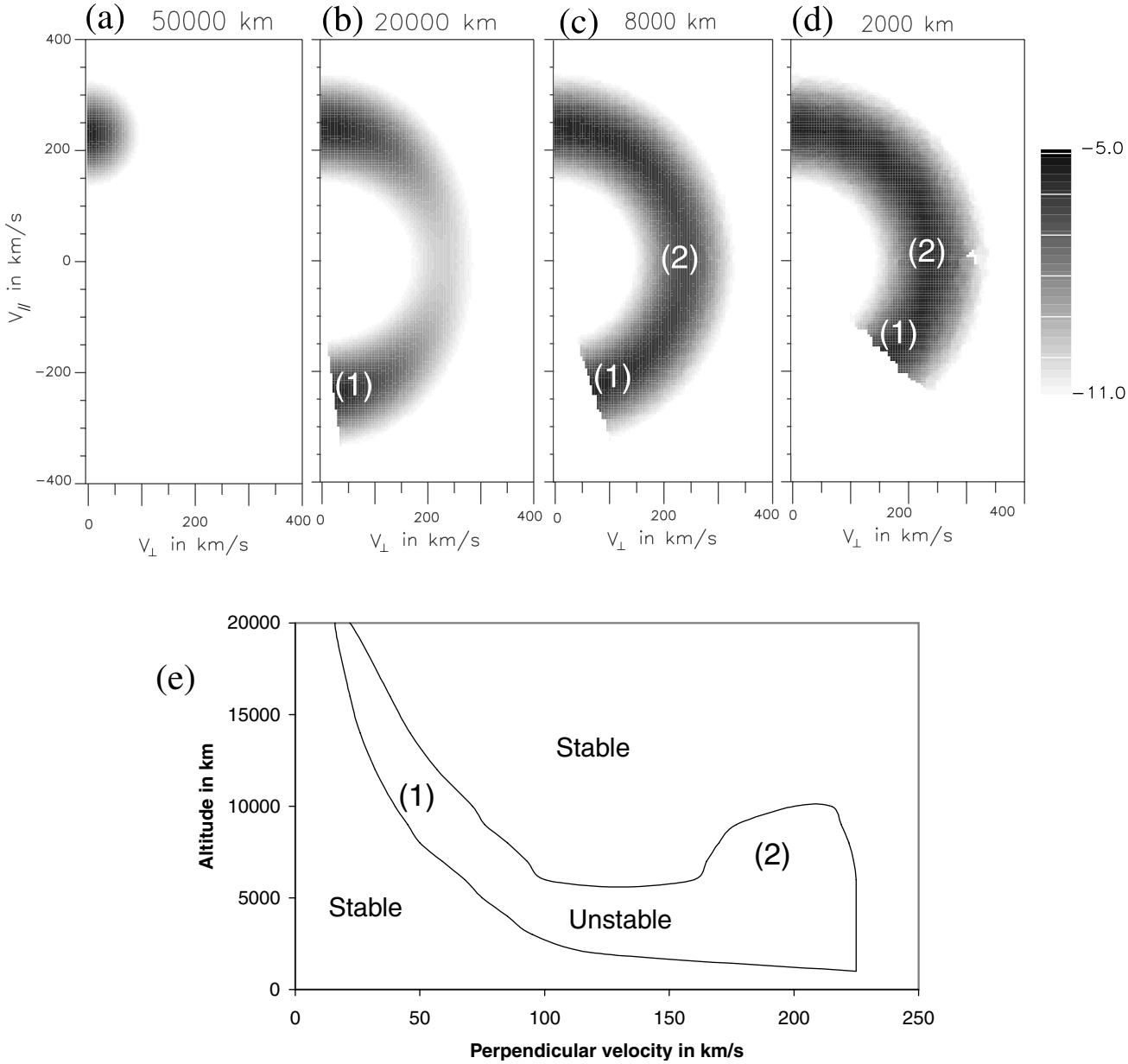

Figure 11. Results of the modeled injected populations, including the resulting velocity space H^+ ring distribution in $(\text{km s}^{-1})^{-3}$ normalized to unit at different altitudes: (a) 50,000 km, (b) 20,000 km, (c) 8000 km, and (d) 2000 km. (e) The regions of positive perpendicular gradient versus perpendicular velocity and altitude. This is obtained by integrating the ring distribution $f(V_{//}, V_{\perp})$ over the parallel velocities.

the low-energy component of the magnetosheath population. The altitude domain of the cumulative heating scenario coincides with the altitude range where the ring distribution may destabilize LH waves over a broad range of perpendicular velocities. However, the velocity threshold required for LH heating is a few tens of km s^{-1} and comparable to or greater than the velocities of the H^+ and O^+ outflowing ions observed by Hyperboloid over the polar cap. Therefore such outflowing ions are more plausibly heated by waves in the BBELF range at lower altitudes.

5. Discussion

[34] On the basis of the main results, which are presented in the previous sections, Figure 13 displays a possible steady state heating scenario to be operative in the cusp for this data set. This scenario supports the idea that LHCP ion cyclotron heating occurs in the cusp in a wide altitude range from ~1000 up to at least 15,000 km, while cusp LH heating is controlled by the characteristics of the ion ring distributions and may contribute to strong ion energization between 2000 and 10,000 km in altitude.

[35] An approximate calculation has shown in section 3 that the LHCP ion cyclotron component of the BBELF waves may preheat ionospheric ions and provide sufficient energies to be followed by LH heating higher up. By referring to previous observations by the Freja [*Norqvist et al.*, 1998] and FAST [*Lund et al.*, 2000] satellites in the same altitude range, most of the transverse ion heating observations are associated with enhanced BBELF emissions. The efficiency of the previous ion energization mechanism may be verified by comparing the upward ion energy flux to the total

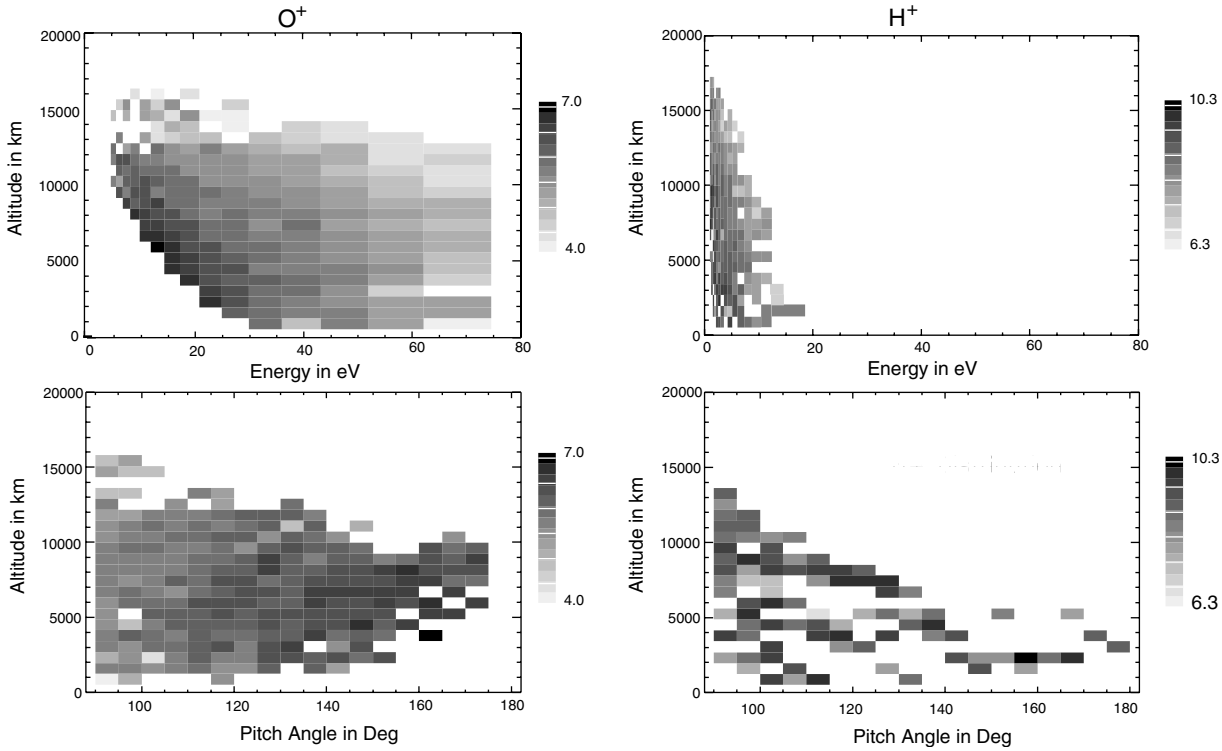

Figure 12. Simulation results for O^+ and H^+ ions, including (top) energy-altitude distributions and (bottom) pitch angle-altitude distributions, reconstituted along the poleward boundary of the heating region. The gray scales correspond to the number of fluxes per unit energy range in $(m^2 s\ sr\ eV^2)^{-1}$.

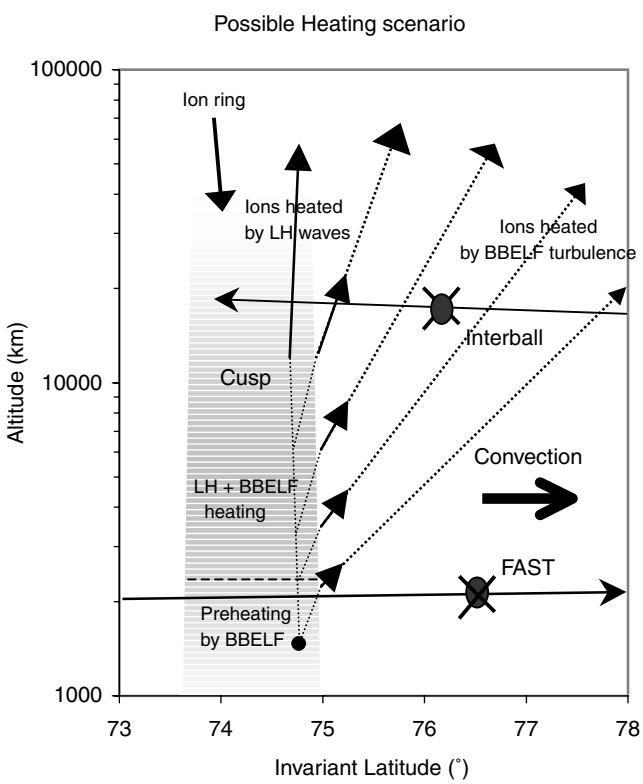

Figure 13. Picture of the heating scenario occurring inside the polar cusp versus altitude and latitude. Solid lines correspond to the satellite trajectories. Dashed lines correspond to examples of ion trajectories with a vector length proportional to the velocity.

Poynting flux. The O^+ energy flux at FAST altitude can be estimated by taking an average energy of 20 eV, an average upward velocity of 3 km s^{-1}, and a density of $10^3 cm^{-3}$, which gives 10 $\mu W\ m^{-2}$ (15 $\mu W\ m^{-2}$ at 1000 km). Unfortunately, we cannot estimate directly the Poynting flux associated with the LHCP ion cyclotron component because magnetic wave field measurements were unavailable at the ion gyrofrequencies. However, we can estimate the total Poynting flux by taking the electric and magnetic wave fields at lower frequencies to be ~30 mV m^{-1} and 10 nT, respectively. This gives an energy flux of 240 $\mu W\ m^{-2}$, of which a few percent is enough to produce the observed transverse ion heating at FAST altitude.

[36] At low altitude, ion energization by DC parallel electric (E) field may occur in the cusp [*Pfaff et al.*, 1998]. However, analysis of the low-energy component of the ion distributions along the poleward heating boundary shows the presence of low-energy (few eV) heated protons at altitudes up to 15,000 km, suggesting that upward E fields cannot prominently operate. Conversely, the characteristics of the ion conic distribution at FAST altitude show a weak pressure cooker effect, consistent with a small downward E field. Using the formula derived by *Jasperse and Grossbard* [2000], we infer a downward E field about a few $\mu V\ m^{-1}$, which is rather small compared to the values in downward auroral current regions (K. Lynch, private communication, 2001). However, in addition to the gravity, such E fields may slow low-energy ionospheric ions down on reaching higher altitudes [*Jasperse and Grossbard*, 2000]. An estimation of the ion-heating rates at FAST points out that LHCP ion cyclotron heating is much more efficient in heating heavy ions, according to the theory [*Chang et al.*, 1986]. However, from the same estimations, LH waves are dominant in heating H^+ ions, while for O^+ ions, LH heating seems less significant than LHCP ion cyclotron heating. This result is consistent with Monte Carlo simulations performed by *André et al.* [1994] and applied to an event where both BBELF and LH waves are observed by the Freja

satellite at 1700 km in altitude. It was shown that this two-wave component mechanism may reproduce the shape of the (H^+ and O^+) ion conics. Particularly, because of the velocity threshold in the LH-heating rate profile, such a mechanism contributes to the formation of a high-energy tail in the ion distributions. Furthermore, a model of the characteristics of the ion ring distribution versus altitude emphasizes that such distributions are unstable from ~2000 up to 10,000 km in altitude and contain a wide range of unstable perpendicular velocities from ~50 up to 230 km s^{-1}. This result agrees with previous observations on the S3-3 and DE 1 satellites [*Roth and Hudson*, 1985], which highlighted LH transverse heating generated by ion ring distributions inside the cusp at altitudes ranging from 1 to 4 Earth radii. However, such a threshold effect in perpendicular velocity implies that LH heating becomes important at higher energies and may produce ionospheric ions with energies about a few keV. The effect of the magnetospheric convection is negligible for such ions, which have shorter times of flight (a few minutes). Therefore these are observed inside the cusp at the Interball AP altitude. Furthermore, the contribution of LH waves to the cusp heating can be investigated by comparing the incoming proton energy flux from the magnetopause to the outgoing O^+ and H^+ energy fluxes at Interball AP altitude. The proton energy flux is inferred from the model used in section 3 by taking an average downward velocity $V_b = 230$ km s^{-1} and a density $n_b = 2 \times 10^{-3}$ cm^{-3}. This gives an energy flux of 0.025 μW m^{-2} at 8 R_E in altitude (10 μW m^{-2} at 1000 km), of which a fraction is transferred to the ionospheric ions through LH heating. From ion measurements by the ION experiment aboard Interball AP inside the cusp region, the upward $H^+$and O^+ ion energy fluxes are found both ~0.5 μW m^{-2}at 19,000 km in altitude (20 μW m^{-2} at 1000 km). These values are higher than the energy flux carried by the magnetosheath ion injections but smaller than the Poynting flux carried by BBELF waves. These comparisons point out that other mechanisms such as the preheating by waves in the BBELF range contribute to ion energization in the cusp region. This result is consistent with adiabatic trajectories of low-energy ions, as performed in section 4, showing that such outflowing ions have velocities that are smaller than the threshold required for LH heating. The fact that LH waves act as an additional process is also consistent with statistical studies on FAST by *Lund et al.* [2000], who argue that most of the transverse ion heating events below 4000 km in altitude are associated with enhanced BBELF emissions, while the correlation with intense emissions in the very low frequency (VLF) range, such as LH waves, is poor. However, a statistical study of the energy fluxes carried by the precipitating protons and the outflowing populations is warranted in order to investigate the occurrence of LH heating in the cusp.

[37] Other sources of free energy may contribute to ion outflows in the cusp, particularly at ionospheric altitudes (a few hundreds of kilometers). By studying an event of intense terrestrial outflows associated with the passage of a coronal mass ejection (CME), *Moore et al.* [1999b] showed that the magnitude of the outflow is correlated with dynamic pressure fluctuations in the solar wind. However, any specific mechanism for generating ion outflow by dynamic pressure fluctuations was given. Another possible source of free energy is the electromagnetic energy (Poynting flux) supplied by the transport of reconnected field lines from the magnetopause to the ionosphere. From the same event as that reported by *Moore et al.* [1999b], *Strangeway et al.* [2000] proposed a scenario where the Poynting flux is dissipated through frictional heating into the ionosphere. Such a mechanism is a first step to produce ion outflows by increasing the ionospheric scale height and then allowing access of ionospheric ions to the altitudes where heating by BBELF waves can occur. From five consecutive cusp crossings by FAST the authors showed a good correlation between the maximum Poynting flux and the maximum outflowing energy flux. For our case study we do not investigate the contribution of frictional heating to the outflow. Since particle measurements are unavailable at ionospheric altitudes, such investigations are not possible from a single case study using remote analysis from FAST. However, as suggested by *Strangeway et al.* [2000], a statistical analysis is warranted to study this scenario.

6. Conclusions

[38] We have presented an event of low-energy outflowing ions observed by the Hyperboloid experiment aboard Interball AP from 13,000- to 19,000-km altitude coincident with convection field measurements from a pair of SuperDARN radars. Low-energy outflowing H^+ and O^+ populations are observed over the dayside morning polar cap by Interball AP. Both data sets emphasize that the convection patterns act as a crucial parameter in locating the source of the ion-heating processes that have occurred at lower altitude. Simultaneously, the cusp crossing by the FAST satellite at 2000 km in altitude has provided information about the nature of the ion-heating processes and the characteristics of the plasma populations at a lower altitude. FAST data have shown that not only one energization mechanism can occur in the cusp region. For this case study, ion outflows are associated with transverse ion heating correlated with enhanced BBELF emissions as well as an intense electrostatic turbulence around the LH frequency. Since the electron population has insufficient energies to drive a LH wave unstable, linear instability analysis pointed out that LH waves are destabilized by ion ring distributions, originating from magnetosheath proton injections. An investigation of the altitude dependence of LH heating by modeling the ion injections into the cusp shows that for our data set the contribution of LH waves to strong ion energization is important. However, from an analysis of the heating rates as a function of the ion velocity, the BBELF turbulence is needed as a preheating mechanism so that LH heating is able to occur. From Interball AP data, because of the velocity threshold effect of the LH-heating rate, the BBELF turbulence dominates the production of low-energy outflowing ions, which are drifted by the convection into the polar cap region.

[39] On the basis of statistical observations of transverse ion-heating events in the auroral regions by FAST [*Lund et al.*, 2000], a correlation with enhanced LH emissions seems unusual. Such a mechanism generated by magnetosheath ion injections is more common to the polar cusp, as suggested by DE 1 observations [*Roth and Hudson*, 1985]. To support this idea, additional work including a significant number of conjunctions between Interball AP and FAST in the enlarged cusp/cleft region is warranted. Because the motion of heated ions inside the heating region is nonadiabatic, kinetic and Monte Carlo simulations of quasi-linear transverse heating by LHCP ion cyclotron and LH waves will be performed to model the wave-particle interactions producing the ionospheric ion outflow. This is one way to determine in a quantitative manner the contribution of the different wave mechanisms to the heating versus altitude and to study the historical effects of the ionospheric flux tubes that are convected outside the heating regions. This will be the subject of a future paper.

[40] **Acknowledgments.** The Interball Project was accomplished in the frame of contract N025-7535/94 with the Russian Space Agency (RKA). The Hyperboloid experiment was financially supported by CNES under the auspices of grants covering the period 1985–2000. FAST data analysis at the University of California in Berkeley was supported through NASA grant NAG5-3596. The Saskatoon and Kapuskasing radars are operated, respectively, by the Institute of Space and Atmospheric Studies at the University of Saskatchewan, Canada, and by the Applied Physics Laboratory at the Johns Hopkins University in Laurel, Maryland. The conjunction between Interball AP and the Saskatoon/Kapuskasing pair has been identified using V. Prokhorenko calculations at IKI, Moscow, Russia.

[41] Janet G. Luhmann thanks the referees for their assistance in evaluating this paper.

References

Abramowitz, M., and I. A. Stegun, *Handbook of Mathematical Functions*, Dover, Mineola, N. Y., 1964.

Akimoto, K., K. Papadopoulos, and D. Winske, Lower-hybrid instabilities driven by an ion velocity ring, *J. Plasma Phys.*, *34*, 445, 1985.

Amatucci, W. E., D. N. Walker, G. Ganguli, D. Duncan, J. A. Antoniades, J. H. Bowles, V. Gavrishchaka, and M. E. Koepke, Velocity-shear-driven ion cyclotron waves and associated transverse ion heating, *J. Geophys. Res.*, *103*, 11,711, 1998.

André, M., H. Koskinen, and L. Matson, Local transverse ion energization in and near the polar cusp, *Geophys. Res. Lett.*, *15*, 107, 1988.

André, M., G. B. Crew, W. K. Peterson, A. M. Persoon, C. J. Pollock, and M. J. Engebretson, Ion heating by broadband low-frequency waves in the cusp/cleft, *J. Geophys. Res.*, *95*, 20,809, 1990.

André, M., P. Norqvist, A. Vaivads, L. Eliasson, O. Norberg, A. I. Eriksson, and B. Holback, Transverse ion energization and wave emissions observed by the Freja satellite, *Geophys. Res. Lett.*, *21*, 1915, 1994.

Bell, T. F., U. S. Inan, V. S. Sonwalkar, and R. A. Helliwell, DE-1 observations of lower hybrid waves exited by VLF whistler mode waves, *Geophys. Res. Lett.*, *18*, 393, 1991.

Bingham, R., B. J. Kellett, R. A. Cairns, R. O. Dendy, and P. K. Shulka, Wave generation by ion horseshoe distributions on auroral field lines, *Geophys. Res. Lett.*, *26*, 2713, 1999.

Burch, J. L., P. H. Reiff, R. A. Heelis, J. D. Winningham, W. B. Hanson, C. Guirgolo, J. D. Menietti, R. A. Hoffman, and J. N. Barfield, Plasma injection and transport in the mid-altitude polar cusp, *Geophys. Res. Lett.*, *9*, 921, 1982.

Carlson, C. W., R. F. Pfaff, and J. G. Watzin, The fast auroral snapshot (FAST) mission, *Geophys. Res. Lett.*, *25*, 2013, 1998.

Chang, T., and B. Coppi, Lower hybrid acceleration and ion evolution in the suprauroral region, *Geophys. Res. Lett.*, *8*, 1253, 1981.

Chang, T., G. B. Crew, N. Hershkowitz, J. R. Jasperse, J. M. Retterer, and J. D. Winningham, Transverse acceleration of oxygen ions by electromagnetic ion cyclotron resonance with broad band left-hand polarized waves, *Geophys. Res. Lett.*, *13*, 636, 1986.

Dubouloz, N., M. Bouhram, C. Senior, D. Delcourt, M. Malingre, and J.-A. Sauvaud, Spatial structure of the cusp/cleft ion fountain: A case study using a magnetic conjugacy between Interball AP and a pair of SuperDARN radars, *J. Geophys. Res.*, *106*, 261, 2001.

Erlandson, R. E., L. J. Zanetti, M. H. Acuna, A. Eriksson, L. Eliasson, M. H. Boehm, and L. Blomberg, Freja observations of electromagnetic ion cyclotron (ELF) waves and transverse oxygen ion acceleration on auroral field lines, *Geophys. Res. Lett.*, *21*, 1855, 1994.

Gorney, D. J., An alternative interpretation of ion ring distributions observed by the S3-3 satellite, *Geophys. Res. Lett.*, *10*, 417, 1983.

Greenwald, R. A., et al., A global view of the dynamics of high latitude convection, *Space Sci. Rev.*, *71*, 761, 1995.

Jasperse, J. R., and N. Grossbard, The Alfven-Falthammar formula for the parallel *E* field and its analogue in downward auroral-current regions, *IEEE Trans. Plasma Sci.*, *28*, 1874, 2000.

Knudsen, D. J., B. A. Whalen, T. Abe, and A. Yau, Temporal evolution and spatial dispersion of ion conics: Evidence for a polar cusp heating wall, in *Solar System Plasmas in Space and Time, Geophys. Monogr. Ser.*, vol. 84, edited by J. L. Burch and J. H. Waite, pp. 163–169, AGU, Washington, D.C., 1994.

Krall, N. A., and A. W. Trivelpiece, *Principles of Plasma Physics*, San Francisco Press, Calif., 1986.

Lockwood, M., M. O. Chandler, J. L. Horwitz, J. H. Waite, Jr., T. E. Moore, and C. R. Chappell, The cleft ion fountain, *J. Geophys. Res.*, *90*, 9736, 1985a.

Lockwood, M., J. H. Waite, Jr., T. E. Moore, J. F. E. Johnson, and C. R. Chappell, A new source of suprathermal O+ ions near the dayside polar cap boundary, *J. Geophys. Res.*, *90*, 4099, 1985b.

Lund, E. J., et al., Transverse ion acceleration mechanisms in the aurora at solar minimum: Occurrence distributions, *J. Atmos. Terr. Phys.*, *62*, 467, 2000.

Moore, T. E., M. Lockwood, M. O. Chandler, J. H. Waite Jr., C. R. Chappell, A. Persoon, and M. Sugiura, Upwelling O+ ion source characteristics, *J. Geophys. Res.*, *91*, 7019, 1986.

Moore, T. E., R. Lundin, D. Alcayde, M. André, S. B. Ganguli, M. Temerin, and A. Yau, Source processes in the high-altitude ionosphere, *Space Sci. Rev.*, *88*, 7, 1999a.

Moore, T. E., W. K. Peterson, C. T. Russell, M. O. Chandler, M. R. Collier, H. L. Collin, P. D. Craven, R. Fitzenreiter, B. L. Gilles, and C. J. Pollock, Ionospheric mass ejection in response to a coronal mass ejection, *Geophys. Res. Lett.*, *26*, 2339, 1999b.

Newell, P. T., and C.-I. Meng, The cusp and the cleft/boundary layer: Low-altitude identification and statistical local time variation, *J. Geophys. Res.*, *93*, 14,549, 1988.

Newell, P. T., W. J. Burke, E. R. Sanchez, C.-I. Meng, M. E. Greenspan, and C. R. Clauer, The low-latitude boundary layer and the boundary plasma sheet at low altitude: Prenoon precipitation regions and convection reversal boundaries, *J. Geophys. Res.*, *96*, 21,013, 1991.

Norqvist, P., M. André, L. Eliasson, A. I. Eriksson, L. Blomberg, H. Lühr, and J. Clemmons, Ion cyclotron heating in the dayside magnetosphere, *J. Geophys. Res.*, *101*, 13,179, 1996.

Norqvist, P., M. André, and M. Tyrland, A statistical study of ion energization mechanisms in the auroral region, *J. Geophys. Res.*, *103*, 23,459, 1998.

Onsager, T. G., C. A. Kletzing, J. B. Austin, and H. MacKiernan, Model of magnetosheath plasma in the magnetosphere: Cusp and mantle particles at low-altitudes, *Geophys. Res. Lett.*, *20*, 479, 1993.

Peterson, W. K., A. W. Yau, and B. A. Whalen, Simultaneous observations of H^+ and O^+ ions at two altitudes by the Akebono and Dynamics Explorer 1 satellites, *J. Geophys. Res.*, *98*, 11,177, 1993a.

Peterson, W. K., et al., Observations of a transverse magnetic field perturbation at two altitudes on the equatorward edge of the magnetospheric cusp, *J. Geophys. Res.*, *98*, 21,463, 1993b.

Pfaff, R., et al., Initial FAST observations of acceleration processes in the cusp, *Geophys. Res. Lett.*, *25*, 2037, 1998.

Retterer, J. M., T. Chang, and J. R. Jasperse, Particle acceleration by intense auroral VLF turbulence, in *Physics of Space Plasmas*, edited by T. Chang, G. B. Crew, and J. R. Jasperse, p. 119, Sci. Publishers, Cambridge, England, 1989.

Roth, I., and M. K. Hudson, Particle simulations of electrostatic emissions near the lower hybrid frequency, *J. Geophys. Res.*, *88*, 483, 1983.

Roth, I., and M. K. Hudson, Lower hybrid heating of ionospheric ions due to ion ring distributions in the cusp, *J. Geophys. Res.*, *90*, 4191, 1985.

Staciewicz, K., Y. Khotyaintsev, M. Berthomier, and J.-E. Wahlund, Identification of widespread turbulence of dispersive Alfvén waves, *Geophys. Res. Lett.*, *27*, 173, 2000.

Strangeway, R. J., C. T. Russell, C. W. Carlson, J. P. McFadden, R. E. Ergun, M. Temerin, D. M. Klumpar, W. K. Peterson, and T. E. Moore, Cusp field-aligned currents and ion outflows, *J. Geophys. Res.*, *105*, 21,129, 2000.

Wahlund, J.-E., et al., Broadband ELF plasma emission during auroral energization, 1, Slow ion acoustic waves, *J. Geophys. Res.*, *103*, 4343, 1998.

M. Berthomier, C. W. Carlson, and I. Roth, Space Science Laboratory, University of California, Berkeley, CA 94720, USA.

M. Bouhram, D. Delcourt, M. Malingre, R. Pottelette, and C. Senior, Centre d'étude des Environnements Terrestre et Planétaires, 94100 Saint-Maur, France. (mehdi.bouhram@cetp.ipsl.fr)

N. Dubouloz, Laboratoire de Physique et Chimie de l'Environnement, 3A Avenue de la Recherche Scientifique, Orléans, 45071 France.

J. R. Jasperse, Air Force Research Laboratory, Hanscom AFB, MA 01731-3010, USA.

J.-A. Sauvaud, Centre d'étude Spatiale des Rayonnements, 31028 Toulouse cedex 4, France.

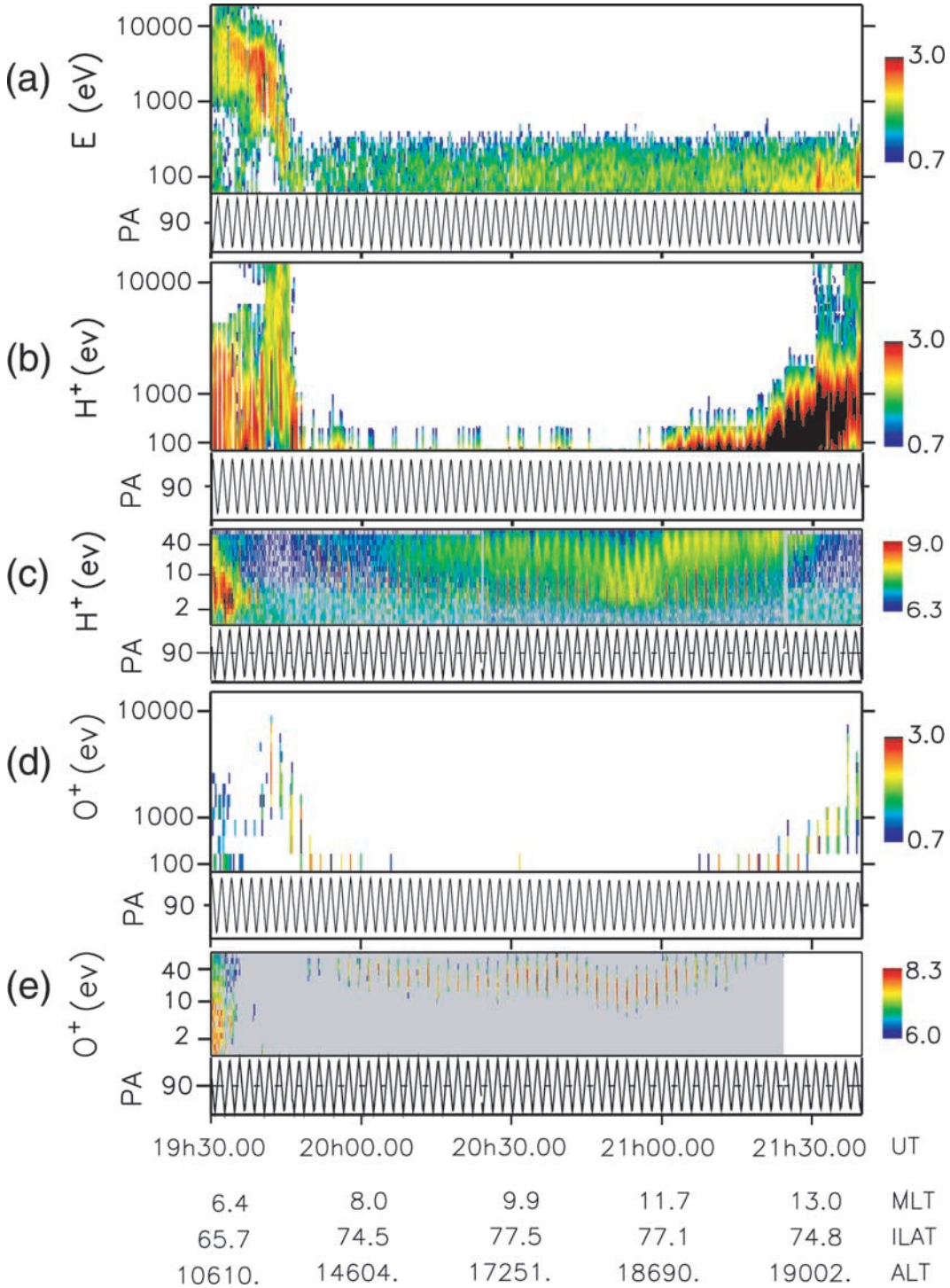

Figure 2. Energy-time spectrograms of particles aboard Interball AP on January 17, 1998, between 1930 and 2140 UT. (a) 100 eV to 10 keV electrons, (b) 100 eV to 10 keV H^+ ions, (c) 0–80 eV H^+ ions, (d) 100 eV to 10 keV O^+ ions, and (e) 0–80 eV O^+ ions. High-energy measurements in counts are from the ION experiment. Low-energy ion number fluxes in log $[(m^2\ s\ sr\ eV)^{-1}]$ are measured by the central window of the Hyperboloid experiment. The corresponding pitch angle (PA) plot is represented below each spectrogram.

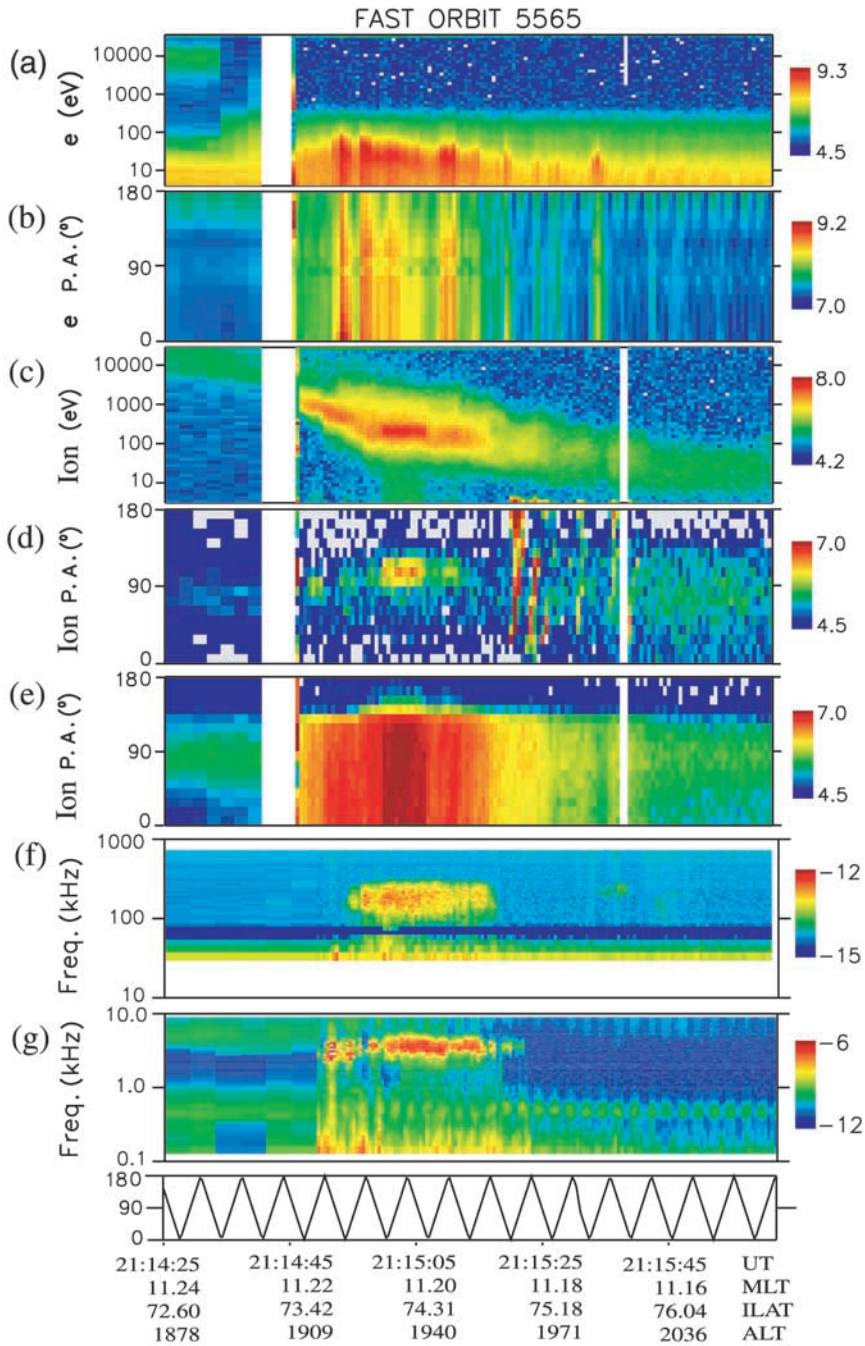

Figure 4. FAST observations of a cusp crossing on January 17, 1998, between 2114:25 and 2116:05 UT. (a) The electron energy spectra from 3 eV to 30 keV for all pitch angles, (b) the electron pitch angle spectra for all energies, (c) the ion energy spectra from 3 eV to 30 keV for all pitch angles, (d) the ion pitch angle spectra integrated over energies below 20 eV, and (e) the ion pitch angle spectra integrated over energies above 60 eV. All particle energy fluxes are in log [eV $(cm^2\ s\ sr\ eV)^{-1}$]. Note that fluxes near 180° are upgoing and those near 0° are downgoing. (f) The high-frequency electric field wave power spectrum and (g) the low-frequency perpendicular electric field wave spectrum. All wave spectra are in log [$V^2m^{-2}\ Hz^{-1}$]. The angle between the antenna and the geomagnetic field is shown below the spectra.